

AI-driven Conservative-to-Primitive Conversion in Hybrid Piecewise Polytropic and Tabulated Equations of State

Semih Kacmaz and Roland Haas

*Department of Physics, University of Illinois Urbana-Champaign, Urbana, Illinois 61801, USA and
National Center for Supercomputing Applications,
University of Illinois Urbana-Champaign, Urbana, Illinois 61801, USA*

E. A. Huerta

*Data Science and Learning Division, Argonne National Laboratory, Lemont, Illinois 60439, USA
Department of Computer Science, The University of Chicago, Chicago, Illinois 60637, USA and
Department of Physics, University of Illinois Urbana-Champaign, Urbana, Illinois 61801, USA*

(Dated: December 12, 2024)

We present a novel AI-based approach to accelerate conservative-to-primitive inversion in relativistic hydrodynamics simulations, focusing on hybrid piecewise polytropic and tabulated equations of state. Traditional root-finding methods are computationally intensive, particularly in large-scale simulations. To address this, we employ feedforward neural networks (NNC2PS and NNC2PL), trained in PyTorch and optimized for GPU inference using NVIDIA TensorRT, achieving significant speedups with minimal loss in accuracy. The NNC2PS model achieves L_1 and L_∞ errors of 4.54×10^{-7} and 3.44×10^{-6} , respectively, with the NNC2PL model yielding even lower error values. TensorRT optimization ensures high accuracy, with FP16 quantization offering 7x faster performance than traditional root-finding methods. Our AI models outperform conventional CPU solvers, demonstrating enhanced inference times, particularly for large datasets. We release the scientific software developed for this work, enabling the validation and extension of our findings. These results highlight the potential of AI, combined with GPU optimization, to significantly improve the efficiency and scalability of numerical relativity simulations.

I. INTRODUCTION

In numerical relativity, accurately modeling astrophysical systems such as neutron star mergers relies on solving the equations of relativistic hydrodynamics, which involve the inversion of conservative-to-primitive (C2P) variable relations [1–3]. This process, central to simulations of general relativistic hydrodynamics (GRHD), typically requires computationally expensive root-finding algorithms, such as Newton-Raphson methods, and interpolation of complex, multi-dimensional equations of state (EOS) tables [4, 5]. These methods, while robust, incur significant computational costs and can lead to inefficiencies, particularly in large-scale simulations, where up to billions of C2P calls may be required per time step. This limitation is especially pronounced in simulations that aim to produce accurate gravitational waveforms for sources that may be detected by gravitational wave detectors like Advanced LIGO, where the accuracy of the results must be achieved efficiently and within feasible computational times [6–13].

Recent advances have explored the potential of machine learning (ML) to replace traditional root-finding approaches in this context [14]. Specifically, neural networks have shown promise in accelerating the C2P inversion process while maintaining high accuracy [14]. Building on this, the present work introduces a novel approach that leverages ML to accelerate the recovery of primitive variables from conserved variables in relativistic hydrodynamics simulations, with particular focus on hybrid piecewise polytropic and tabulated EOS. These EOS

models provide more realistic descriptions of the dense interior of neutron stars, yet their complexity makes the traditional C2P procedure very computationally expensive.

We present a suite of feedforward neural networks trained to directly map conserved variables to primitive variables, bypassing the need for traditional iterative solvers. In particular, we employ a hybrid approach, utilizing the flexibility of neural networks to handle the challenges posed by complex EOS models. Our models are implemented using modern deep learning tools, such as PyTorch, and optimized for GPU inference with NVIDIA TensorRT [15, 16]. Through comprehensive performance benchmarking, we demonstrate that our approach significantly outperforms traditional numerical methods in terms of speed, particularly when using mixed-precision deployment on modern hardware accelerators like the NVIDIA A100 GPU.

We also quantify the scalability of our ML models, demonstrating near-linear scaling for large datasets and substantial reductions in inference times, even for datasets containing hundreds of thousands of data points. These results highlight the potential of ML-based methods to enable high-accuracy, high-throughput simulations, positioning them as an essential tool for next-generation numerical relativity codes. By accelerating the C2P inversion, our approach facilitates the more efficient generation of gravitational waveforms, directly contributing to the ongoing efforts to better understand and characterize the behavior of dense astrophysical systems. Accurate numerical relativity simulations of bi-

nary neutron star mergers are critical for advancing our understanding of the complex dynamics of these events. These simulations provide unique insights into the highly nonlinear interplay between gravitational waves, matter, and nuclear physics, particularly in the extreme environments surrounding such mergers [17, 18]. By comparing simulation results with gravitational wave observations, we can probe the EOS of dense nuclear matter, offering constraints on the properties of neutron star interiors [19, 20]. Moreover, these simulations enable the exploration of fundamental microphysics, such as the behavior of matter at supra-nuclear densities, shedding light on phenomena like hyperons, quark matter, and nuclear phase transitions [21, 22]. Thus, by enhancing computational efficiency, our approach not only accelerates waveform generation but also advances the ability to explore the intricate physics of compact binary mergers, enabling more comprehensive studies of these astrophysical phenomena.

This article is structured as follows. Section II introduces the EOS considered in this study, along with the methodologies employed for designing, training, validating, and testing the ML models. In Section III, we present our key results, including an assessment of the accuracy of the ML models across different model types and quantization schemes. Additionally, we provide a comparison of the computational performance of the ML models relative to traditional root-finding methods. Finally, Section IV offers a summary of the findings and outlines potential avenues for future research.

II. METHODS

We present a ML-based model with the potential to accelerate recovery of primitive variables from conserved variables in general relativistic hydrodynamics simulations, specifically focusing on scenarios employing hybrid piecewise polytropic EOS, and tabulated EOS. As in traditional approaches, this conversion requires inverting the conservative-to-primitive map, a process often reliant on computationally expensive root-finding algorithms. While previous work has demonstrated the success of machine learning for this task with the Γ -law EOS [23], here we investigate its application to hybrid piecewise polytropic EOS, which offers a more realistic representation of neutron star interiors, as well as the tabulated EOS, which incorporate current nuclear physics model of neutron matter. To evaluate the performance of our neural network, we use a traditional CPU-based root-finding algorithm (provided by the *RePrimAnd* library [24]) as a baseline for comparison. Our aim is to demonstrate the speed advantages of the neural network approach for conservative-to-primitive variable conversion. Our network is implemented using PyTorch, and the inference speed tests are performed using *libtorch* and NVIDIA TensorRT's C++ API.

In general relativity, the equations of relativistic hy-

drodynamics can be expressed in a conservation form suitable for numerical implementation. Specifically, in a flat spacetime, they constitute the following first-order, flux-conservative hyperbolic system:

$$\frac{1}{\sqrt{-g}} \left(\frac{\partial \sqrt{\gamma} \mathbf{u}}{\partial x^0} + \frac{\partial \sqrt{-g} \mathbf{F}^i(\mathbf{u})}{\partial x^i} \right) = \mathbf{0}, \quad (1)$$

where $g = \det(g_{\mu\nu})$ is the metric determinant, and $\gamma = \det(\gamma_{ij})$ is the determinant of the three-metric induced on each spacelike hypersurface. The state vector of the conserved variables is $\mathbf{u} = (D, \mathbf{S}_j, \tau)$, and the flux vector is given by

$$\mathbf{F}^i = \left(D \left(v^i - \frac{\beta^i}{\alpha} \right), S_j \left(v^i - \frac{\beta^i}{\alpha} \right) + p \delta_j^i, \right. \\ \left. \tau \left(v^i - \frac{\beta^i}{\alpha} \right) + p v^i \right),$$

where α is the lapse function and β^i the spacelike shift vector: two kinematic variables describing the evolution of spacelike foliations in spacetime as in a typical $3 + 1$ (ADM) formulation.

The five quantities satisfying Eq. 1, all measured by an Eulerian observer sitting at a spacelike hypersurface, are the relativistic rest-mass density, D , the three components of the momentum density, S_j , and the energy density relative to the rest mass density, $\tau = E - D$, respectively. These are related to the primitive variables; rest-mass density, ρ , three-velocity, v_i , specific internal energy, ϵ , and pressure, p through

$$D = \rho W, \\ S_j = \rho h W^2 v_j, \\ \tau = \rho h W^2 - p - D, \quad (2)$$

where $W = 1/\sqrt{1 - \gamma_{ij} v^i v^j}$ is the Lorentz factor, and $h = 1 + \epsilon + p/\rho$ is the specific enthalpy.

Incorporating the EOS into the picture provides the thermodynamical information linking the pressure to the fluid's rest-mass density, and internal energy, which combined with the definitions above, closes the system of equations given in Eq. 1 [25–27].

We will first focus on the hybrid piecewise polytropic EOS. The hybrid piecewise polytropic EOS was introduced for simplified simulations of stellar collapse to model the stiffening of the nuclear EOS at nuclear density, and include thermal pressure during the postbounce phase [28]. In gravitational-wave science, it is more commonly used as described in Read et al. [29], where it enables gravitational-wave parameter estimation and waveform modeling by effectively capturing macroscopic neutron star observables with minimal parameters. The structure of this EOS consists of multiple cold polytropes, defined by parameters $K_0, K_1, \dots, K_{\text{nsegments}-1}$ and $\Gamma_0, \Gamma_1, \dots, \Gamma_{\text{nsegments}-1}$, where **nsegments** denotes the total number of segments. Additionally, it includes

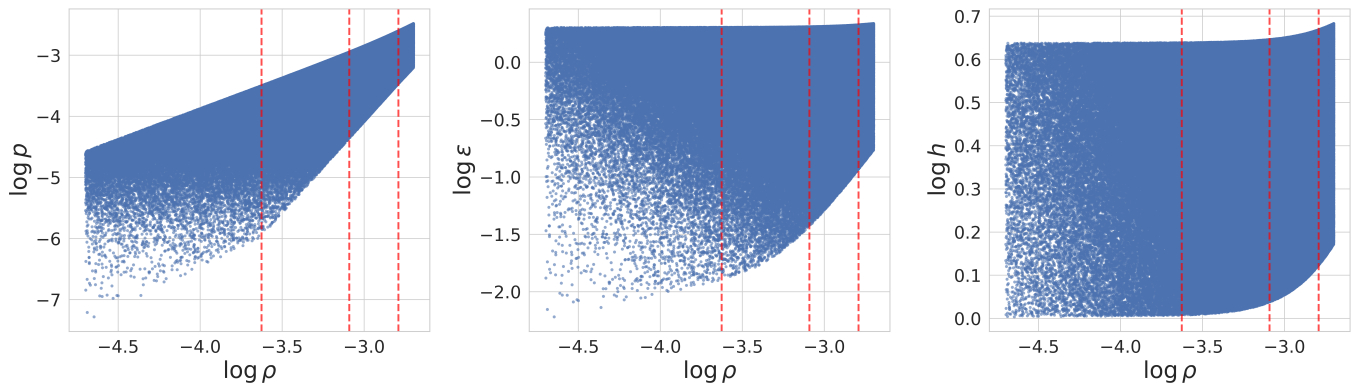


FIG. 1: Visualization of the thermodynamic relations based on the complete training data generated for the four-segment piecewise polytropic EOS-based model. From left to right: pressure (p) vs. rest-mass density (ρ), specific internal energy (ϵ) vs. rest-mass density (ρ), and specific enthalpy (h) vs. rest-mass density (ρ). All quantities are plotted on a logarithmic scale. The distinct segments of the piecewise polytropic EOS are delineated by the red vertical lines.

a thermal Γ -law component characterized by Γ_{th} . Continuity of pressure and internal energy across segments, in accordance with the first law of thermodynamics, is ensured after appropriately setting initial values for the polytropic indices, density breakpoints (denoted ρ_{breaks}), and other relevant parameters. In this context, pressure and specific internal energy components in each density interval are given by

$$\begin{aligned}
 p_{\text{cold}} &= K_i \rho^{\Gamma_i}, \\
 \epsilon_{\text{cold}} &= a_i + \frac{K_i}{\Gamma_i - 1} \rho^{\Gamma_i - 1}, \\
 p_{\text{th}} &= (\Gamma_{\text{th}} - 1) \rho (\epsilon - \epsilon_{\text{cold}}), \\
 p &= p_{\text{th}} + p_{\text{cold}},
 \end{aligned} \tag{3}$$

where a_i is segment-specific constant, and the rest mass density, ρ , is assumed to fall into the segments specified by each of ρ_{breaks} .

In addition to the hybrid piecewise polytropic EOS-based model, we will train a separate network to infer the conservative-to-primitive transformation utilizing the tabulated EOS data. Specifically, we will use the Lattimer-Swesty EOS with a compressibility parameter $K = 220$ (hereafter will be referred to as, LS220 EOS), due to its prevalence and historical significance. Our training dataset is based on a modern, updated version of LS220 EOS constructed and made available by Schneider, Roberts, and Ott in a more recent study [30].

Below, we outline the dataset preparation, model architecture, training process, and methods used in inference speed testing with `libtorch` and NVIDIA TensorRT to evaluate computational efficiency.

A. Data

1. Piecewise Polyotropic EOS Based Model Data

We generate a dataset of 500,000 samples using geometrized units where $G = c = M_{\odot} = 1$. Without loss of generality, we furthermore use a Minkowski metric $g_{\mu\nu} = \text{diag}(-1, +1, +1, +1)$. The rest-mass density, ρ , is sampled uniformly from $[2 \times 10^{-5}, 2 \times 10^{-3}]$, and the fluid's three-velocity is assumed one-dimensional along the x -axis, sampled uniformly from $v_x \in [0, 0.721]$. A four-segment piecewise polytrope is used, with segment-wise polytropic indices $\Gamma = [1.3569, 3.0050, 2.9880, 2.8510]$. The first segment's polytropic constant, K_0 , is set to 8.9493×10^{-2} . Subsequent polytropic constants, K_i , are determined by enforcing pressure continuity. Similarly, the first segment's constant, a_0 , is set to zero, while subsequent a_i values ensure continuity of internal energy. The density breaks for the segments are specified at $\rho = 2.3674 \times 10^{-4}$, 8.1147×10^{-4} , and 1.6191×10^{-3} . The thermal component has an adiabatic index of $\Gamma_{\text{th}} = 5/3$. Additionally, the thermal component of the specific internal energy, ϵ_{th} , is sampled uniformly from $[0, 2]$. A structured dataset is then constructed by converting the primitive variables to conserved variables using the standard relativistic hydrodynamic relations given in Eq. 2. In this dataset, conserved variables serve as input features, and the pressure is the target variable. The resulting dataset is then split into training, validation, and test sets, with each set fully standardized to zero mean and unit variance to ensure equal contribution of all features during neural network training (Fig. 1).

2. Tabulated EOS Based Model Data

To generate the training data for the tabulated EOS-based model, we sample from a provided EOS table and follow a procedure similar to the one described in Section II A 1. We begin by reading in the EOS table, which contains the variables electron fraction (Y_e), temperature (T), rest-mass density (ρ), specific internal energy (ϵ), and pressure (p). These quantities are stored in logarithmic form in the table and are extracted accordingly. For each data point, a random one-dimensional three-velocity, v_x , is sampled from the interval $[0, 0.721)$, and values are randomly chosen for electron fraction, temperature, and density from among the tabulated values. Using these, the corresponding values of ρ , ϵ , and p are then fetched from the EOS table. The primitive variables are then converted into conserved variables using standard relativistic hydrodynamics relations given in Eq. 2. A total of 1,000,000 datapoints are generated using this process [31]. Similar to the hybrid piecewise polytropic EOS-based model, the data is split into training, validation, and test sets, with each set fully standardized to zero mean and unit variance before being used for neural network training.

B. Model architecture

1. Piecewise Polytropic EOS Based Model

For the hybrid piecewise polytropic EOS-based model, we tested two feedforward neural networks of varying complexity to represent the conservative-to-primitive variable transformation. Each network takes as input the three conserved variables (D, S_x, τ) (Eq.2) and outputs the pressure p (Eq.3), assuming the remaining momentum density components are zero for simplicity. After experimenting with multiple multi-layer perceptron (MLP) architectures, we identified two models that offered a good balance between accuracy, speed, and trainability. The smaller model, `NNC2PS`, features two hidden layers with 600 and 200 neurons, while the larger model, `NNC2PL`, contains five hidden layers with 1024, 512, 256, 128, and 64 neurons (Fig 2).

ReLU activation functions were applied to the hidden layers to introduce nonlinearity, with the output layer kept linear. We found these models strike an effective balance between complexity and performance, making them well-suited for our task.

2. Tabulated EOS Based Model

For the tabulated EOS-based model, we use a single feedforward neural network, `NNC2P_Tabulated`, to achieve an inherently equivalent task with minor differences. This model takes as input the log-scaled variables ($\log D, \log S_x, \log \tau, \log Y_e$) and outputs the log-

scaled pressure, $\log p$ (Eq.3), assuming S_y and S_z are zero for simplicity as before. Using log-scaled inputs and outputs aligns with the format of the tabulated EOS values, which are also stored in logarithmic form to accommodate the typically large values of these physical quantities. This approach reduces the range of feature magnitudes, facilitating more stable learning dynamics and better alignment with the source data.

We explored several MLP architectures, varying in parameters, layers, and training strategies, to identify an optimal design for our task. Among these, a structure resembling `NNC2PL`, detailed in Section II B 1 above, emerged as a robust choice. This architecture effectively balanced capacity and efficiency, enabling accurate learning of log-scaled pressure from tabulated EOS data (Fig. 2).

C. Training approach

We use a similar procedure to optimize all neural networks: `NNC2PS`, `NNC2PL`, and the tabulated baseline model, `NNC2P_Tabulated`, with minor tweaks. Training was performed on a single NVIDIA A100 GPU on the Delta cluster. For the hybrid piecewise polytropic EOS-based models (`NNC2PS` and `NNC2PL`), we employed a custom, physics-informed loss function that penalizes negative pressure predictions. This loss function is a modified mean-squared error:

$$\mathcal{L}(\theta) = \frac{1}{n} \sum_{i=1}^n (\hat{y}_i(\theta) - y_i)^2 + q \cdot \sum_{i=1}^n \text{ReLU}(-\mathcal{N}^{-1}(\hat{y}_i(\theta))),$$

where $\hat{y}_i(\theta)$ represents the network's estimation for feature i , y_i is the corresponding target value, ReLU is the familiar rectified linear unit defined by $\text{ReLU}(x) = \max(0, x)$, and $\mathcal{N}^{-1}(\cdot)$ represents an inverse normalization procedure based on the training data statistics. The penalty factor, q , was optimized for each model, with $q = 150$ for `NNC2PS` and $q = 350$ for `NNC2PL`. These values consistently suppressed negative pressure predictions on the test set. For the tabulated EOS model (`NNC2P_Tabulated`), the structure of the data precluded negative predictions, so a standard mean-squared error loss function was used.

All models were trained using the Adam optimizer with an initial learning rate of 3×10^{-4} . A learning rate scheduler reduced the learning rate by a factor of 0.5 if the validation loss failed to improve for five consecutive epochs. `NNC2PS` and `NNC2PL` were trained for 85 epochs, while `NNC2P_Tabulated` required 250 epochs. For each epoch, the model was set to training mode, and data was loaded in batches of 32 onto the GPU. This batch size was chosen based on experimentation to balance the number of epochs and overall time to convergence. While training with larger batches and multiple GPUs (using PyTorch's `DataParallel` module or other approaches) is possible, we found no significant advantage regarding the

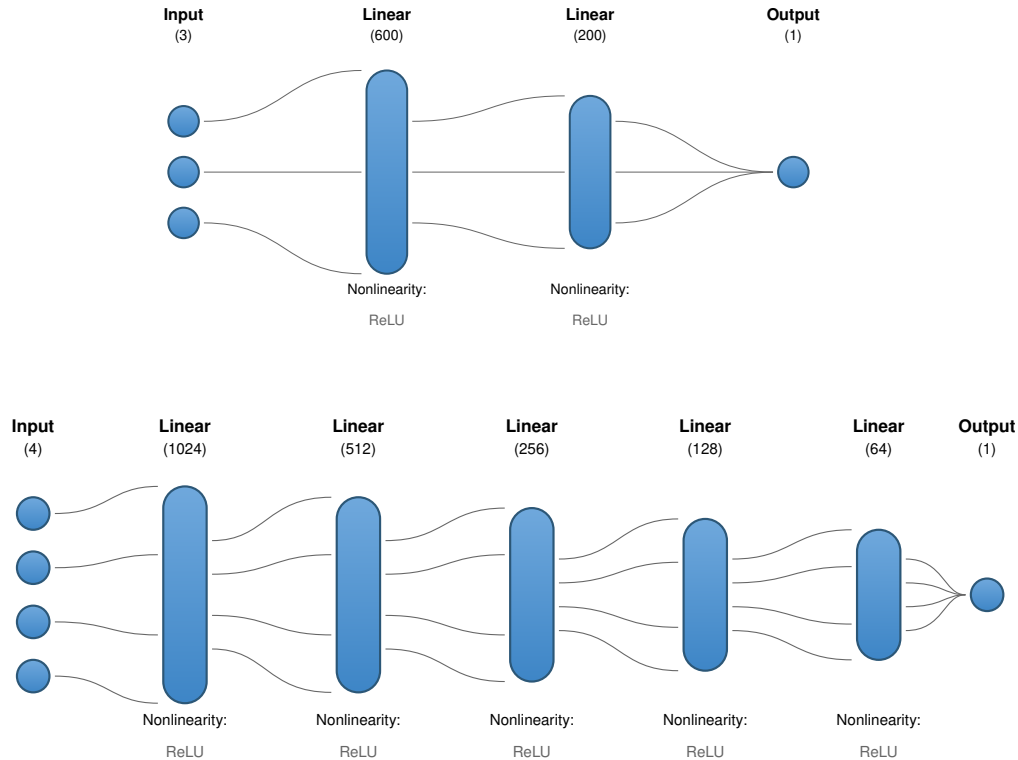


FIG. 2: Architectures of the neural networks used for conservative-to-primitive variable mapping. Top: The NNC2PS network takes conserved variables D , S_x , and τ as input and outputs the pressure p . Bottom: The NNC2P_Tabulated network uses the logarithm of conserved variables $\log D$, $\log S_x$, and $\log \tau$, along with the electron fraction Y_e , as input, outputting the logarithm of pressure $\log p$. The NNC2PL network (not shown) shares a similar architecture to NNC2P_Tabulated but with the same input/output structure as NNC2PS.

total time to convergence and ultimately opted for this simpler, more portable approach. For each batch, optimizer gradients were reset before generating predictions, and the loss was computed using respective loss functions. Backpropagation was then performed to update the model parameters.

After completing the training phase for each epoch, the model’s performance is evaluated on the validation dataset, accumulating the validation loss similarly to the training loss. Both losses are normalized by the size of the respective datasets and stored for further analysis, specifically for clues of potential overtraining.

D. Inference Speed Tests

In our inference speed tests, we evaluated two main approaches for efficient deployment: a TorchScript model, and NVIDIA’s TensorRT optimized engines. These tests were conducted to measure and compare inference speed under typical deployment conditions, aiming to take advantage of the A100 GPU on Delta.

1. TorchScript Deployment

To prepare models for inference with TorchScript, we first saved a scripted version of the model, which is compatible with PyTorch’s JIT compiler, optimizing runtime execution without modifying the model’s core structure. TorchScript’s scripting provides some degree of optimization, enabling faster model execution than standard PyTorch models but without the hardware-level optimizations that TensorRT offers.

2. TensorRT Deployment

For TensorRT, we explored both FP32 (unquantized) and FP16-quantized engines, ultimately deciding not to pursue INT8 quantization due to accuracy degradation observed in initial tests. After extensive testing, we opted for dynamic engine building with batch sizes up to approximately 25,000, as this configuration provided the best balance between performance and flexibility for our hardware and model structure. It must be noted

that constructing an optimal engine in TensorRT is a nuanced process, influenced by multiple factors including model architecture, hardware specifications, intended batch sizes during inference, and input data. Therefore, achieving the best results often involves iterative tuning and profiling to adapt the engine to the specific deployment environment and workload requirements. Below, we summarize the overall engine-building process we followed in detail:

- **Model Export to ONNX:** First, we exported the PyTorch model to the ONNX format. This conversion enables interoperability with TensorRT, which uses ONNX as its primary model input format.
- **TensorRT Engine Building:** Using TensorRT’s Python API, we constructed both FP32 and FP16 engines. A logger was initialized for verbose logging to capture potential issues during engine building. With the `TensorRT Builder`, we created a network definition with explicit batch handling, which is essential for dynamic batching configurations.
- **Parsing and Validating the ONNX Model:** We loaded the ONNX model into TensorRT, where the `OnnxParser` validated and parsed the model. Parsing errors, if any, were logged for troubleshooting, ensuring a valid model structure before optimization.
- **Configuration and Optimization Profiles:** The `BuilderConfig` was set with a 2 GB workspace memory limit, balancing memory usage and speed. We set up a dynamic optimization profile specifying minimum, optimal, and maximum batch sizes, tailored to accommodate varying input sizes efficiently. This profile allowed the engine to handle batch sizes dynamically, with an optimal batch size close to our expected usage, while allowing flexibility to adapt for both smaller and larger input volumes.
- **Engine Serialization:** Finally, we serialized and saved the engine, creating a portable and optimized binary that can be loaded for deployment. This step encapsulates the model’s architecture, weights, and optimizations, ensuring it is ready for fast inference.

Overall, the process of optimizing and saving models using both TorchScript and TensorRT gave us insight into balancing flexibility, accuracy, and performance. For larger batch sizes and greater computational demands, TensorRT’s dynamic engine approach in FP16 is often more effective, even for models as simple as ours, while TorchScript remains a reliable fallback and simpler alternative.

For the actual inference speed test procedure, we implemented two distinct workflows on a single GPU for

both approaches. The TorchScript-based approach required no special configuration beyond loading the model and executing it in batches. It utilized `libtorch` to load the model directly, allowing straightforward GPU deployment and batch processing.

For the TensorRT-based approach, however, several additional configurations were required. The model, after conversion to an optimized engine, was loaded using TensorRT’s C++ API. This process required close attention to low-level CUDA memory management through TensorRT’s `executeV2` function, setting up input and output buffers manually, and optimizing precision settings (such as enabling half-precision FP16) to enhance performance. While TensorRT’s setup was more complex, it promises to enable significant inference speed improvements by utilizing hardware-specific optimizations.

III. RESULTS

1. Accuracy

Table I summarizes the accuracy results based on L_1 and L_∞ error metrics for each model variant—`NNC2PS`, `NNC2PL`, and `NNC2P_Tabulated`—including both the unquantized and quantized TensorRT engines built from them.

TABLE I: Accuracy Results for All Models

Model	L_1 Error	L_∞ Error
<code>NNC2PS</code> (PyTorch)	4.54×10^{-7}	3.44×10^{-6}
<code>NNC2PS</code> (TensorRT)	4.54×10^{-7}	3.43×10^{-6}
<code>NNC2PS</code> (TensorRT-FP16)	6.39×10^{-7}	8.98×10^{-6}
<code>NNC2PL</code> (PyTorch)	2.75×10^{-7}	2.61×10^{-6}
<code>NNC2PL</code> (TensorRT)	2.88×10^{-7}	2.69×10^{-6}
<code>NNC2PL</code> (TensorRT-FP16)	5.32×10^{-7}	9.84×10^{-6}
<code>NNC2P_Tabulated</code> (PyTorch)	8.02×10^{-3}	3.54×10^{-1}
<code>NNC2P_Tabulated</code> (TensorRT)	8.16×10^{-3}	3.45×10^{-1}
<code>NNC2P_Tabulated</code> (TensorRT-FP16)	1.38×10^{-2}	7.44×10^{-1}

The `NNC2PS` model trained in PyTorch achieves very high accuracy with an L_1 error of 4.54×10^{-7} and an L_∞ error of 3.44×10^{-6} . When the model is converted to a TensorRT engine, the accuracy remains nearly identical, with an L_1 error of 4.54×10^{-7} and an L_∞ error of 3.43×10^{-6} , indicating minimal loss in precision due to TensorRT optimization. However, when FP16 quantization is applied, the error rates increase to an L_1 error of 6.39×10^{-7} and an L_∞ error of 8.98×10^{-6} , revealing an obvious side-effect of reduced precision.

The larger `NNC2PL` model, rather expectedly, achieves lower L_1 and L_∞ errors than `NNC2PS`, with an L_1 error of 2.75×10^{-7} and an L_∞ error of 2.61×10^{-6} . The corresponding TensorRT engine preserves this high level of accuracy, showing only a slight and negligible increase to an L_1 error of 2.88×10^{-7} and L_∞ error of 2.69×10^{-6} respectively. The FP16 quantized version, however, sees

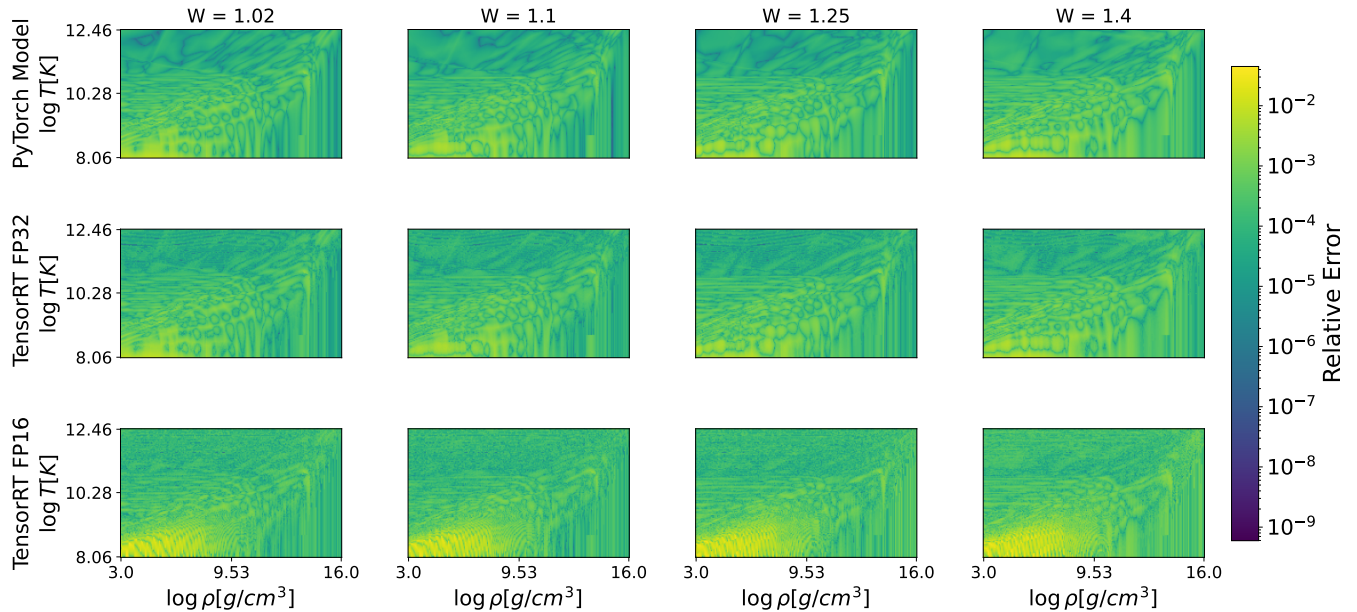


FIG. 3: Relative error of the `NNC2P_Tabulated` model for various Lorentz factors (W) with $Y_e \approx 0.1$. The plots highlight the accuracy trends across different regions of the LS220 EOS table, showing larger relative errors in low-density and low-temperature regions, reflecting the inherent complexities of the EOS in this region. This behavior is consistent across the tested W values of 1.02, 1.1, 1.25, and 1.4 and is more pronounced for the FP16 precision TensorRT engine.

a notable rise in error metrics, with an L_1 error of 5.32×10^{-7} and an L_∞ error of 9.84×10^{-6} .

The `NNC2P_Tabulated` model exhibits an L_1 error of 8.02×10^{-3} and an L_∞ error of 3.54×10^{-1} . It should be noted that the apparent order-of-magnitude difference in its accuracy does not indicate inferiority or failure of the model; in fact, it is the result of the simple fact that this model is trained on a completely different dataset constructed from the LS220 EOS table to estimate the logarithmic pressure values. The TensorRT engine version also shows only a slight increase in L_1 error to 8.16×10^{-3} . With FP16 quantization, the L_1 error rises, again, more noticeably to 1.38×10^{-2} .

Additionally, we examined the relative accuracy of the `NNC2P_Tabulated` model for parameters $W = 1.02, 1.1, 1.25,$ and 1.4 with $Y_e \approx 0.1$ (See Fig. 3). The relative error, defined as the absolute error divided by the true value for each point in a specific parameter set, was not uniform across the parameter space. Larger relative errors were observed in the lowest density and temperature regions of the EOS table, while slightly smaller errors occurred in the high-temperature regions. This accuracy trend was consistent across all tested Lorentz factor (W) values and even more emphasized for the FP16 precision TensorRT engine. The LS220 EOS, as provided by [30], transitions from detailed treatment at high densities to simplified approximations at lower densities, which may contribute to these disparities. Low-density regions are

inherently challenging due to the dominance of thermal effects, non-uniform phase transitions, and the treatment of nuclear matter surfaces, which can exacerbate modeling errors [30, 32]. These characteristics likely explain the reduced accuracy in these regions, where variations in the nuclear matter's phase state are more pronounced.

The overall results show that TensorRT's optimizations maintain accuracy across models when using full precision. FP16 quantization, while accelerating inference (as will be discussed further below), introduces higher error rates, particularly in certain models. The potential trade-off between the inference speed and precision can be especially important in relativistic hydrodynamics simulations, where the accuracy of small-scale structures and wave propagation can critically impact the fidelity of predictions. For such simulations, even slight deviations due to quantization can influence results, making full-precision TensorRT inference particularly valuable when accuracy is paramount. Conversely, FP16 quantization may be suitable for faster, lower-fidelity simulations where minor accuracy trade-offs are acceptable.

2. Inference Speed Analysis

The inference speed of various approaches was analyzed using a single NVIDIA A100 GPU for neural network models and a CPU implementation of the numer-

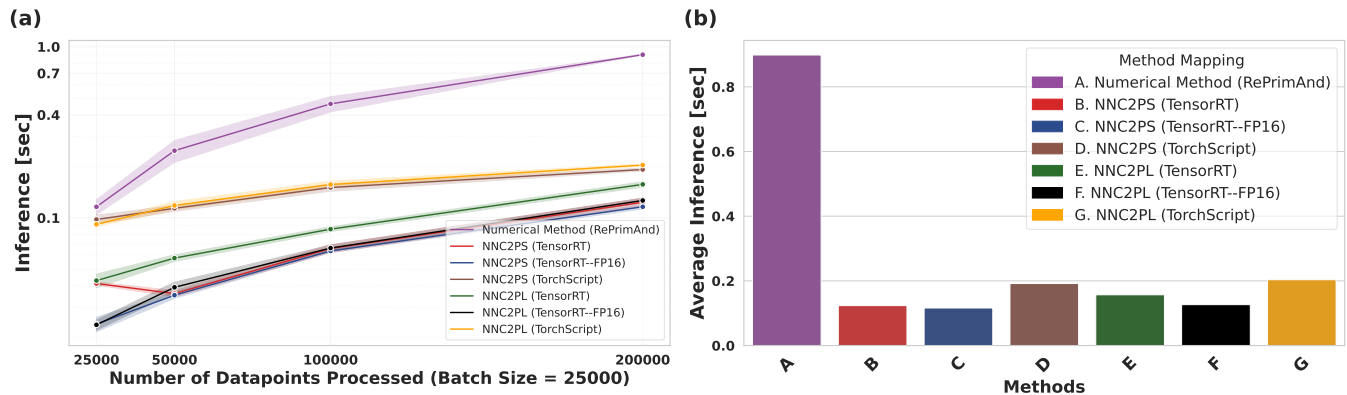


FIG. 4: Inference speed comparison of various C2P inversion methods. (a) Inference time as a function of dataset size for a traditional numerical solver (*RePrimAnd* on a single CPU) and two neural network models (NNC2PS and NNC2PL) using TensorRT (FP32 and FP16 precision) and TorchScript on a single NVIDIA A100 GPU. (b) Inference speed comparison for a 200,000 data point dataset, highlighting the performance gains achieved with TensorRT, particularly with FP16 optimization.

ical method, as in the *RePrimAnd* library, to represent traditional simulation techniques. Each setup was tested across multiple dataset sizes ranging from 25,000 to 200,000 data points, with ten inference runs conducted per configuration to ensure stability and consistency in the results, as can be seen in Fig. 4(a).

RePrimAnd-based implementation of the numerical method executed all computations on a CPU and demonstrated nearly linear scaling with respect to the size of the dataset. While it performed adequately for smaller datasets, the approach became increasingly time-consuming for larger datasets. For 200,000 datapoints, for example, it was almost 8 times slower than the fastest TensorRT engine (See Fig. 4(b)).

The neural network-based methods NNC2PS and NNC2PL were deployed in three configurations: using TensorRT with both FP32 and FP16 precision modes, and utilizing TorchScript format. All configurations utilized the NVIDIA A100 GPU for acceleration. Neural networks deployed in full precision with TensorRT consistently (and expectedly) delivered faster inference times than the numerical method, achieving substantial improvements even for the largest datasets. However, the computational requirements of full precision meant that the performance gains were modest compared to the optimized FP16 configuration. Mixed-precision deployments in TensorRT offered the most significant performance gains across all dataset sizes. In this configuration, both NNC2PS and NNC2PL achieved substantial reductions in inference time compared to full precision. The FP16 optimizations allowed these models to process datasets ranging from 25,000 to 200,000 data points with remarkable efficiency, showcasing their suitability for large-scale applications. Finally, as a general-purpose deployment pipeline, TorchScript demonstrated reliable inference capabilities, but its performance lagged behind TensorRT in both precision configurations.

In numerical relativistic hydrodynamics simulations, the mapping of conserved variables to primitive variables often occurs tens of millions of times, underscoring the critical need for efficient inference strategies. While highly optimized multi-threaded CPU implementations, such as those achievable with the *RePrimAnd* library, can utilize up to 128 CPUs on platforms like Delta, GPU-based methods nonetheless offer a compelling alternative due to their massive parallelism. The inherent parallel architecture of GPUs enables the concurrent processing of large data batches, directly addressing the bottleneck posed by the numerous C2P calls required in large-scale simulations. Our results (Fig.4) demonstrate that TensorRT optimizations, particularly FP16 precision, further enhance GPU performance by enabling faster computations with minimal accuracy loss (Table I). Furthermore, multi-GPU deployments, while not explored in this work, hold the potential to scale performance even further for the massive datasets characteristic of numerical relativity. While our single-GPU benchmarks do not demonstrate a decisive advantage over the single-core CPU implementation using *RePrimAnd* at the dataset scales tested, the observed trends in inference speed, coupled with ongoing advancements in GPU technology and software, suggest a promising outlook for GPU-based C2P solvers as dataset sizes and model complexities continue to increase.

IV. CONCLUSIONS

This work presents a novel method for accelerating C2P inversions in relativistic hydrodynamics simulations, focusing on hybrid piecewise polytropic and tabulated equations of state. We employ AI-driven techniques, specifically feedforward neural networks coupled with TensorRT optimization, to achieve significant per-

formance improvements compared to traditional CPU solvers. Our results demonstrate that this approach offers a compelling alternative to computationally demanding iterative methods while maintaining a reasonably high accuracy.

Future research could explore several avenues for extending and refining this approach. This includes adapting the models to a broader class of equations of state and investigating alternative network architectures to further enhance performance. Continued exploitation of TensorRT, including additional optimization strategies and parallel implementations across multiple GPUs, offers the potential for even greater reductions in computational time for C2P inversions. These advancements could enable more efficient and detailed simulations of complex astrophysical systems. We anticipate that AI-driven methods, particularly those incorporating TensorRT, will be instrumental in advancing GRHD simulations, and the field of numerical relativity, in general. We release the software needed to validate and extend our findings at the following GitHub repository [33].

V. ACKNOWLEDGEMENTS

E.A.H. gratefully acknowledges support from National Science Foundation award OAC-1931561 and OAC-2209892. R.H. gratefully acknowledges support from Natural Science Foundation award OAC-2103680, OAC-2004879, OAC-2310548, OAC-2005572, and OAC-2411068. This research used the Delta advanced computing and data resource which is supported by the National Science Foundation (award OAC 2005572) through ACCESS-CI [34] allocation PHY160053. Delta is a joint effort of the University of Illinois Urbana-Champaign and its National Center for Supercomputing Applications. This research used the DeltaAI advanced computing and data resource, which is supported by the National Science Foundation (award OAC 2320345) and the State of Illinois. DeltaAI is a joint effort of the University of Illinois Urbana-Champaign and its National Center for Supercomputing Applications. We further acknowledge the use of Matplotlib [35] and Seaborn [36] for the generation of figures in this publication.

-
- [1] S. C. Noble, C. F. Gammie, J. C. McKinney, and L. Del Zanna, “Primitive Variable Solvers for Conservative General Relativistic Magnetohydrodynamics,” *Astrophys. J.*, vol. 641, no. 1, pp. 626–637, Apr. 2006.
- [2] J. A. Faber and F. A. Rasio, “Binary neutron star mergers,” *Living Reviews in Relativity*, vol. 15, no. 1, pp. 1–83, 2012.
- [3] M. D. Duez, Y. T. Liu, S. L. Shapiro, and B. C. Stephens, “Relativistic magnetohydrodynamics in dynamical spacetimes: Numerical methods and tests,” *Phys. Rev. D*, vol. 72, no. 2, p. 024028, Jul. 2005.
- [4] J. A. Font, “Numerical Hydrodynamics in General Relativity,” *Living Reviews in Relativity*, vol. 3, no. 1, p. 2, Dec. 2000.
- [5] P. Chang and Z. Etienne, “General relativistic hydrodynamics on a moving-mesh I: static space-times,” *Mon. Not. Roy. Astron. Soc.*, vol. 496, no. 1, pp. 206–214, 2020.
- [6] D. Radice, S. Bernuzzi, and A. Perego, “The dynamics of binary neutron star mergers and gw170817,” *Annual Review of Nuclear and Particle Science*, vol. 70, no. 1, p. 95–119, Oct. 2020. [Online]. Available: <http://dx.doi.org/10.1146/annurev-nucl-013120-114541>
- [7] R. Ciolfi, W. Kastaun, B. Giacomazzo, A. Endrizzi, D. M. Siegel, and R. Perna, “General relativistic magnetohydrodynamic simulations of binary neutron star mergers forming a long-lived neutron star,” *Phys. Rev. D*, vol. 95, no. 6, p. 063016, 2017.
- [8] K. Kiuchi, “General relativistic magnetohydrodynamics simulations for binary neutron star mergers,” 5 2024.
- [9] D. M. Siegel and B. D. Metzger, “Three-dimensional general-relativistic magnetohydrodynamic simulations of remnant accretion disks from neutron star mergers: Outflows and r -process nucleosynthesis,” *Phys. Rev. Lett.*, vol. 119, p. 231102, Dec 2017. [Online]. Available: <https://link.aps.org/doi/10.1103/PhysRevLett.119.231102>
- [10] L. Sun, M. Ruiz, S. L. Shapiro, and A. Tsokaros, “Jet launching from binary neutron star mergers: Incorporating neutrino transport and magnetic fields,” *Phys. Rev. D*, vol. 105, no. 10, p. 104028, 2022.
- [11] A. Tsokaros, M. Ruiz, S. L. Shapiro, and K. Uryū, “Magnetohydrodynamic Simulations of Self-Consistent Rotating Neutron Stars with Mixed Poloidal and Toroidal Magnetic Fields,” *Phys. Rev. Lett.*, vol. 128, no. 6, p. 061101, 2022.
- [12] R. Fernández, A. Tchekhovskoy, E. Quataert, F. Foucart, and D. Kasen, “Long-term grmhd simulations of neutron star merger accretion discs: implications for electromagnetic counterparts,” *Monthly Notices of the Royal Astronomical Society*, vol. 482, no. 3, pp. 3373–3393, 2019.
- [13] F. Foucart, R. Haas, M. D. Duez, E. O’Connor, C. D. Ott, L. Roberts, L. E. Kidder, J. Lippuner, H. P. Pfeiffer, and M. A. Scheel, “Low mass binary neutron star mergers: gravitational waves and neutrino emission,” *Physical Review D*, vol. 93, no. 4, p. 044019, 2016.
- [14] T. Dieselhorst, W. Cook, S. Bernuzzi, and D. Radice, “Machine learning for conservative-to-primitive in relativistic hydrodynamics,” *Symmetry*, vol. 13, no. 11, p. 2157, 2021.
- [15] J. Ansel, E. Yang, H. He, N. Gimelshein, A. Jain, M. Voznesensky et al., “Pytorch 2: Faster machine learning through dynamic python bytecode transformation and graph compilation,” in *Proceedings of the 29th ACM International Conference on Architectural Support for Programming Languages and Operating Systems (ASPLOS ’24)*. ACM, apr 2024. [Online]. Available: <https://pytorch.org/assets/pytorch2-2.pdf>
- [16] NVIDIA Corporation, NVIDIA TensorRT, 2024, high-performance deep learning inference engine. [Online]. Available: <https://developer.nvidia.com/tensorrt>

- [17] A. Camilletti, L. Chiesa, G. Ricigliano, A. Perego, L. C. Lippold, S. Padamata, S. Bernuzzi, D. Radice, D. Logoteta, and F. M. Guercilena, “Numerical relativity simulations of the neutron star merger GW190425: microphysics and mass ratio effects,” *Mon. Not. Roy. Astron. Soc.*, vol. 516, no. 4, pp. 4760–4781, 2022.
- [18] T. Dietrich, T. Hinderer, and A. Samajdar, “Interpreting Binary Neutron Star Mergers: Describing the Binary Neutron Star Dynamics, Modelling Gravitational Waveforms, and Analyzing Detections,” *Gen. Rel. Grav.*, vol. 53, no. 3, p. 27, 2021.
- [19] M. Agathos, J. Meidam, W. Del Pozzo, T. G. F. Li, M. Tompitak, J. Veitch, S. Vitale, and C. Van Den Broeck, “Constraining the neutron star equation of state with gravitational wave signals from coalescing binary neutron stars,” *Phys. Rev. D*, vol. 92, no. 2, p. 023012, 2015.
- [20] A. Bauswein, T. W. Baumgarte, and H.-T. Janka, “Prompt merger collapse and the maximum mass of neutron stars,” *Phys. Rev. Lett.*, vol. 111, p. 131101, Sep 2013. [Online]. Available: <https://link.aps.org/doi/10.1103/PhysRevLett.111.131101>
- [21] M. Oertel, M. Hempel, T. Klöhn, and S. Typel, “Equations of state for supernovae and compact stars,” *Rev. Mod. Phys.*, vol. 89, p. 015007, Mar 2017. [Online]. Available: <https://link.aps.org/doi/10.1103/RevModPhys.89.015007>
- [22] M. G. Alford, A. Schmitt, K. Rajagopal, and T. Schäfer, “Color superconductivity in dense quark matter,” *Rev. Mod. Phys.*, vol. 80, pp. 1455–1515, Nov 2008. [Online]. Available: <https://link.aps.org/doi/10.1103/RevModPhys.80.1455>
- [23] T. Dieselhorst, W. Cook, S. Bernuzzi, and D. Radice, “Machine Learning for Conservative-to-Primitive in Relativistic Hydrodynamics,” *Symmetry*, vol. 13, no. 11, p. 2157, Nov. 2021.
- [24] W. Kastaun, J. V. Kalinani, and R. Ciolfi, “Robust Recovery of Primitive Variables in Relativistic Ideal Magnetohydrodynamics,” *Physical Review D*, vol. 103, no. 2, p. 023018, Jan. 2021.
- [25] F. Banyuls, J. A. Font, J. M. Ibáñez, J. M. Martí, and J. A. Miralles, “Numerical $3 + 1$ general relativistic hydrodynamics: A local characteristic approach,” *The Astrophysical Journal*, vol. 476, no. 1, p. 221, feb 1997. [Online]. Available: <https://dx.doi.org/10.1086/303604>
- [26] J. M. Martí and E. Müller, “Numerical Hydrodynamics in Special Relativity,” *Living Reviews in Relativity*, vol. 6, no. 1, p. 7, Dec. 2003.
- [27] J. A. Font, “Numerical Hydrodynamics and Magnetohydrodynamics in General Relativity,” *Living Reviews in Relativity*, vol. 11, no. 1, p. 7, Dec. 2008.
- [28] H.-T. Janka, T. Zwerger, and R. Moenchmeyer, “Does artificial viscosity destroy prompt type-ii supernova explosions?” *Astronomy and Astrophysics (ISSN 0004-6361)*, vol. 268, no. 1, p. 360-368., vol. 268, pp. 360–368, 1993.
- [29] J. S. Read, B. D. Lackey, B. J. Owen, and J. L. Friedman, “Constraints on a phenomenologically parametrized neutron-star equation of state,” *Physical Review D*, vol. 79, no. 12, p. 124032, Jun. 2009.
- [30] A. S. Schneider, L. F. Roberts, and C. D. Ott, “Open-source nuclear equation of state framework based on the liquid-drop model with Skyrme interaction,” *Physical Review C*, vol. 96, no. 6, p. 065802, Dec. 2017.
- [31] T. Wouters, “Machine learning algorithms for the conservative-to-primitive conversion in relativistic hydrodynamics,” M.S. thesis, KU Leuven, 2024.
- [32] S. Bernuzzi, M. Breschi, B. Daszuta, A. Endrizzi, D. Logoteta, V. Nedora, A. Perego, F. Schianchi, D. Radice, F. Zappa, I. Bombaci, and N. Ortiz, “Accretion-induced prompt black hole formation in asymmetric neutron star mergers, dynamical ejecta and kilonova signals,” *Monthly Notices of the Royal Astronomical Society*, vol. 497, no. 2, pp. 1488–1507, Sep. 2020.
- [33] Semih Kacmaz, “C2PNets: Machine Learning for Conservative-to-Primitive Variable Recovery in Numerical Relativity,” 2024, accessed: 2024-12-09. [Online]. Available: <https://github.com/semihkacmaz/C2PNets>
- [34] T. J. Boerner, S. Deems, T. R. Furlani, S. L. Knuth, and J. Towns, “Access: Advancing innovation: Nsf’s advanced cyberinfrastructure coordination ecosystem: Services & support,” in *Practice and Experience in Advanced Research Computing 2023: Computing for the Common Good*, ser. PEARC ’23. New York, NY, USA: Association for Computing Machinery, 2023, p. 173–176. [Online]. Available: <https://doi.org/10.1145/3569951.3597559>
- [35] J. D. Hunter, “Matplotlib: A 2d graphics environment,” *Computing in Science & Engineering*, vol. 9, no. 3, pp. 90–95, 2007.
- [36] M. L. Waskom, “seaborn: statistical data visualization,” *Journal of Open Source Software*, vol. 6, no. 60, p. 3021, 2021. [Online]. Available: <https://doi.org/10.21105/joss.03021>